

High performance InGaAs/InP avalanche photodiode integrated with metal-insulator-metal microcavity

Hao Han

University of Shanghai for Science and Technology

Yicheng Zhu

Shanghai Institute of Technical Physics

Zilu Guo

Shanghai Institute of Technical Physics

Zhifeng Li

Shanghai Institute of Technical Physics

Huidan Qu

Shanghai Institute of Technical Physics

Wantian Gao

Shanghai Institute of Technical Physics

Ding Wang

University of Shanghai for Science and Technology

Wenjuan Wang (✉ wangwj@mail.sitp.ac.cn)

Shanghai Institute of technical physics, Chinese Academy of Sciences <https://orcid.org/0000-0002-6489-8740>

Research Article

Keywords: Avalanche photodiodes, Photoelectric joint simulation, Metal-Insulator-Metal microcavity, Crosstalk

Posted Date: March 13th, 2021

DOI: <https://doi.org/10.21203/rs.3.rs-298600/v1>

License: © ⓘ This work is licensed under a Creative Commons Attribution 4.0 International License.

[Read Full License](#)

Abstract

Reducing the dark current of InGaAs/InP avalanche photodiodes (APDs) is an important way to improve its performance. Decreasing the active size can reduce the dark current but sacrifice the quantum efficiency. In this paper, the Metal-Insulator-Metal (MIM) microcavity is integrated with an APD, which can converge light from tens of microns to several microns, to compensate for the loss of detection efficiency caused by the reduction of the size of the APD. Through photoelectric joint simulation, the optical response of the device can be obtained, and the coupling effect between the MIM structure and the APD can be analyzed directly. The simulation results show that the signal to noise ratio of the APD integrated with the MIM microcavity is twice of the MIM free traditional APD, and the 3dB bandwidth reaches 5.8 GHz. When the MIM microcavity is applied to an APD array, the optical crosstalk between pixels is found to be negligible.

Introduction:

High sensitivity avalanche photodiodes (APDs) are the core component of single photon detection, which are mainly used for quantum key distribution (Albota et al. 2006; Liao et al. 2017) and 3D lidar detection (Marinelli et al. 2018; Yu et al. 2017). Compared with traditional Si APDs, InGaAs / InP APDs have better single photon detection performance in the wavelength range of 1000-1600nm. However, the inherent material defects lead to higher dark count rates(Qiu et al. 2015), which lead to a lower signal-to-noise ratio. Therefore, it is urgent to find an effective method to reduce the dark current (Robert et al. 2009), such as reducing the size of an APD (Carrano et al. 2009), but at the expense of the optical response. In this case, optical lenses are used to compensate for the loss of optical response (Wen et al. 2016; Ou et al. 2018; Sun et al. 2012; Ni et al. 2013). However, in order to obtain a smaller optical spot, the traditional optical lens usually requires a larger diameter and a smaller focal length (Piotrowski et al. 2003; Li et al. 2013; Giuseppe et al. 2015; Petter et al. 2020). At the same time, due to the separation from the APD, it is a huge challenge to achieve a high coupling efficiency (Giuseppe et al. 2015; Petter et al. 2020). In this paper, a metal insulator metal (MIM) optical microcavity is directly integrated on the APD, which is reported in detail in (Wen et al. 2017). The MIM microcavity can collimate and focus the incident light to several microns, and have a high optical transmittance, which provides an effective way to reduce the APD's active diameter to several microns while maintaining a high optical response. Based on the photoelectric joint simulation, the performance of an APD integrated with the MIM microcavity is analyzed directly from the perspective of photoelectric response and the optimal coupling conditions are optimized.

Structure And Simulation:

Fig.1(a) shows the schematic diagram of an InGaAs/InP APD integrated with a MIM microcavity, denoted as MIM-APD. The MIM cavity is directly fabricated on the APD, which consists of three layers: the top Au grating layer, the middle SiO₂ insulator layer, and the bottom Au double slit layer. The lateral boundaries of the cavity are blocked by Au plate, as shown in Fig.1(b). The thickness of Au bars is $t_1 = 100$ nm, and

the insulator is composed of $t_2 = 300$ nm thick SiO_2 . The period of the metallic grating is $p = 1120$ nm, and the Au bar width is $w = 680$ nm. The period number of the top grating is set as 19, and the total length of the MIM cavity along the x -axis is $21 \mu\text{m}$. An InGaAs/InP APD with a separate absorption, grading, charge, and multiplication (SAGCM) structure is denoted in Fig. 1(c). The thicknesses of the multiplication layer, charge layer, and absorption layer are kept as $0.8 \mu\text{m}$, $0.1 \mu\text{m}$, and $1.5 \mu\text{m}$, respectively.

To accurately simulate the optoelectronic coupling effect of the MIM microcavity and the APD, the photoelectric joint simulation is used. First the optical simulation of the MIM-APD is carried out with Ansys Lumerical's Finite Difference Time Domain (FDTD) module (Dennis 2013; Lumerical 2020). TE light with the polarization along x -direction is vertically incident from the top Au grating layer, with a wavelength of 1550 nm, and the power is 10.5 nW. In the optical simulation of the MIM-APD, the photogenerated carrier rate (in the unit of $\text{cm}^{-3}\times\text{s}^{-1}$) in the absorption layer is calculated as the following equation (1) (Crocherie 2009):

$$G = \frac{-\text{Re}(\nabla \cdot \mathbf{P})}{\hbar\nu} = \frac{\sigma|\mathbf{E}|^2}{\hbar\nu} \quad (1)$$

where \mathbf{P} is the Poynting vector, \hbar is the reduced Planck constant, ν is the frequency of light in the absorption layer, σ is the electrical conductivity of the material, and \mathbf{E} is the electric field intensity. Here, we assume that each photon in the APD absorption layer produces generates an electron-hole pair.

Then the electrical simulation of the APD is performed through the CHARGE module (Hurkx et al. 1992; Selberherr 1984) based on carrier drift-diffusion equation and Poisson equation (Dennis 2013), the photogenerated carrier rate G of the absorption layer from the optical simulation is incorporated to obtain the optical response of the MIM-APD. Through the combination of optical and electrical simulation, the optoelectronic coupling effect between the MIM microcavity and the APD can be directly expressed, which is more conducive to the design and optimization of the device. In this paper, 2D simulation is used to save time and computing memory.

Results And Discussion:

The transmission spectrum of the MIM microcavity is shown in Fig. 2(a). The peak transmission located at $1.55 \mu\text{m}$ reaches 60 %. Figure 2(b) and (c) show the electric field distribution through the MIM microcavity. After passing through the top Au grating layer, the incident TE light is transformed into the surface plasmon polariton (SPP) wave, which is y -direction polarized and propagates along $\pm x$. The SPP wave is perfectly confined in the SiO_2 insulator cavity. Through the output slots in the bottom grating layer, the SPP wave in the cavity is transformed into the TE light again. However, the output light from the MIM microcavity has a small divergence angle. Therefore, the distance between the MIM's output holes and the APD's absorption layer directly determines the photoelectric coupling effect.

Figure 2(d) shows a cross section of the MIM-APD. The distance from the bottom grating layer of the MIM cavity to the APD absorption layer is denoted as T , which includes the p^+ InP layer, the InP multiplication layer, the InP charge layer and the InGaAsP layer with tens of nms. Because the thickness of InGaAsP is very thin, we consider it together with InGaAs layer. In order to stabilize the performance of the APD, the thicknesses of the multiplier layer, charge layer and the InGaAs absorption layer are kept as $0.8 \mu\text{m}$, $0.1 \mu\text{m}$, and $1.5 \mu\text{m}$. The thickness of the p^+ InP layer is the only variable. Figure 2(e) shows the energy flux density distribution of the light emitted from the MIM microcavity, with T varying from 1 to $3.5 \mu\text{m}$. We can see that the output light is mainly concentrated in the center, and gradually diverges to both sides with the increase of T . This result means that in the design of the APD, in order to reduce the effective area (denoted as D), it is necessary to make the absorption layer as close to the MIM cavity as possible, so that most of the light can be fully absorbed in the InGaAs absorption layer.

Figure 3 shows the photoresponsivity of the APD, with the punchthrough voltage of 28.9 V . It can be seen that at the same active width D , the photoresponsivity increases with the decrease of T . In addition, as D increases, the photoresponsivity also enlarges. When $T = 1.0 \mu\text{m}$ and D is larger than $6 \mu\text{m}$, the photoresponsivity tends to be saturated, which increases only from 0.585 A/W to 0.610 A/W with D increasing from $6 \mu\text{m}$ to $10 \mu\text{m}$. Therefore, when $T = 1.0 \mu\text{m}$ and $D = 6 \mu\text{m}$, the MIM-APD has the best compromise between D and photoresponsivity. This structure is considered as the best coupling condition for the MIM-APD and is used in the following simulation.

We compare the performance of the optimized MIM-APD with the traditional APD, with the same T as $1 \mu\text{m}$. Figure 4 (a) shows the simulated two-dimensional structure of the MIM-APD with $D = 6 \mu\text{m}$ and the total length of the MIM cavity is $21 \mu\text{m}$. Figure 4 (b) shows the MIM free traditional APD with $D = 21 \mu\text{m}$, and the surface is antireflection coated with a transmittance of 94.8% . Figure 4 (c) shows the simulated I-V curves of the two APDs. When the bias voltage is 30 V , the photocurrents of the traditional APD and the MIM-APD are 9.81 nA and 6.57 nA respectively, and the dark currents are 8.69 pA and 2.54 pA . The decrease of photocurrent in the MIM-APD is mainly due to 60% transmittance of the MIM cavity, as indicated in Fig. (2). In this paper, due to the two-dimensional simulation, the dark current is only proportional to the width of the active region, but for the practical devices, which is proportional to the area of the active region. Therefore, with the decrease of D , the dark current of the MIM-APD will decrease in a square multiple. The signal-to-noise ratio (SNR) of the two APDs is shown in Fig. 4 (d). The SNR of the MIM-APD is twice as that of the traditional APD. At the bias voltage of 28.9 V , the SNRs are 5300 and 2270 , respectively.

In order to analyze the 3dB bandwidth of the APD near the Geiger mode, we performed a transient simulation with a multiplication gain of 85 . The calculated 3-dB bandwidth is shown in in Fig. 4(e). The 3-dB bandwidths of the two APDs are 5.8 GHz and 3.9 GHz , respectively. The 3-dB bandwidth of the MIM-APD is 49% higher than that of the traditional APD, which shows that a smaller D will make a higher 3-dB bandwidth.

When the MIM microcavity is applied to an APD array, the optical crosstalk is analyzed. The whole length of the MIM cavity is $L = 21 \mu\text{m}$, the active width of the APD is $D = 6 \mu\text{m}$, and the distance between the adjacent MIM cavities is $0.5 \mu\text{m}$. The light is incident on the first pixel, we observe the optical response of the adjacent two pixels, as shown in Fig. 5(a). Figure 5 (b) shows the electric field distribution of the three pixels. We can see that the output light from the MIM cavity is mainly concentrated in the first pixel. If an optical transmission monitor is placed on the periphery of the second pixel (around the red frame of crosstalk P1), the optical power is only 0.00138% of the incident light. Figure 5 (c) shows the I-V curves of the three pixels. A small crosstalk current is found at the punchthrough voltage 28.9 V in the second pixel, which is 2.19 pA. Compared with the photocurrent of the first pixel at the same bias voltage, the crosstalk current is only 0.0353% of the photocurrent. The current of the third pixel almost coincides with the dark current. The results show that the crosstalk effect of MIM-APD is almost negligible.

Summary:

The optoelectronic coupling effect of the MIM microcavity and the APD is optimized by the method of the photoelectric joint simulation. Considering a certain divergence angle of the output light from the MIM cavity, the active width of the APD is designed as $6 \mu\text{m}$ and the distance from the MIM bottom layer to the absorption layer is designed as $1 \mu\text{m}$. Compared with the traditional APD, the SNR of the MIM-APD is twice that of the traditional one, and the 3dB bandwidth is increased by 49%. Through optical crosstalk simulation, it's found that the optical crosstalk of the APD array integrated with MIM microcavities is very low, and only the first adjacent pixel has a crosstalk current, which accounts for 0.0353% of the photocurrent. The MIM-APD provides an opportunity for the development of devices with higher sensitivity and higher bandwidth, and also provides a reliable idea for the development of large array APDs with low crosstalk and small pixels.

Declarations

Declarations

Not applicable.

Acknowledgements:

This work was supported by National key R&D Program of China (Grant No. 2016YFB0402404), Natural Science Foundation of China (Grant No. 11991063), Key research project of Frontier Science of Chinese Academy of Sciences (Grant No. QYZDJ-SSW-JSC007), Shanghai Municipal Science and Technology Major Project (Grant No.2019SHZDZX01), and the Strategic Priority Research Program of Chinese Academy of Sciences (Grant No. XDB43010200)

References

- Albota, M.A., Wong, F.N.C., Shapiro, J.H.: Polarization-independent frequency conversion for quantum optical communication. *J. Opt. Soc. Am. B-Opt. Phys.* **25**, 918 (2006).
<https://doi.org/10.1364/JOSAB.23.000918>
- Carrano, J.C., Lambert, D.J.H., Eiting, C.J., Collins, C.J., Campbell, J.C.: Single Photon Avalanche Photodiodes. *Appl. Phys. Lett.* **76**, 924 (2009). <https://doi.org/10.1364/OFC.2009.OWX1>
- Crocherie, A., Boulenc, P., Vaillant, J., Hirigoyen, F., Herault, D., Tavernier, C.: From photons to electrons: a complete 3D simulation flow for CMOS image sensor. *IEEE 2009 International Image Sensor Workshop* (2009). <https://imagesensors.org/2009-papers>
- Dennis, M.S.: *Electromagnetic Simulation Using the FDTD Method*. Wiley-IEEE Press Series (2013).
<https://doi.org/10.1002/9781118646700.ch1>
- Giuseppe, R., Aongus, M., Ryan, W.E., Ren, X., Federica, V., Rudi, L., Andrew, W.J., Mohammad, R.T., Alberto, T., Franco, Z. Gerald, B.S.: Fill-factor improvement of Si CMOS single-photon avalanche diode detector arrays by integration of diffractive microlens arrays. *Opt. Express.* **23**, 33777-33791 (2015).
<https://doi.org/10.1364/OE.23.033777>
- Hurkx, G.A.M., Klaassen, D.B.M., Knuvers, M.P.G.: A new recombination model for device simulation including tunneling. *IEEE Trans. Electron Devices.* **39**, 331 (1992). <https://doi.org/10.1109/16.121690>
- Liao, S.K., Cai, W.Q., Liu, W.Y., Liang, Z., Yang, L.J., Ren, G., Yin, J., Shen, Q., Yuan, C., Li, Z.P.: Satellite-to-ground quantum key distribution. *Phys. Rev. Lett.* **549**, 43 (2017).
<https://doi.org/10.1103/PhysRevLett.119.200501>
- Li, Y., Ye, Z.H., Lin, C., Hu, X.N., Ding, R.J., He, L.: Crosstalk suppressing design of GaAs microlenses integrated on HgCdTe infrared focal plane array. *Opt. Quantum Electron.* **45**, 665-672 (2013).
<https://doi.org/10.1007/s11082-012-9651-3>
- Marinelli, D., Paris, C., Bruzzone, L.: A Novel Approach to 3-D Change Detection in Multitemporal LiDAR Data Acquired in Forest Areas. *IEEE Trans. Geosci. Remote Sensing.* **56**, 3030 (2018).
<https://doi.org/10.1109/TGRS.2018.2789660>
- Ni, X.J., Satoshi, I., Alexander, V.K., Vladimir, M.S.: Ultra-thin, planar, Babinet-inverted plasmonic metalenses. *Light-Sci. Appl.* **2**, 2047 (2013). <https://doi.org/10.1038/lsa.2013.28>
- Ou, K., Li, G.H., Li, T.X., Yang, H., Yu, F.L., Chen, J., Zhao, Z.Y., Cao, G.T., Chen, X.S., Lu, W.: High efficiency focusing vortex generation and detection with polarization-insensitive dielectric metasurfaces. *Nanoscale.* **10**, 19154 (2018). <https://doi.org/10.1039/c8nr07480a>

- Petter, W.R.C., Ren, X., Aongus, M., Hanning, M., Federica, V., Andrew, J.W., Mohammad, R.T., Alberto, Franco, T.Z., Robert, K.H., Gerald, S.B.: High concentration factor diffractive microlenses integrated with CMOS single-photon avalanche diode detector arrays for fill-factor improvement. *Appl. Optics*. **59**, 4488-4498 (2020). <https://doi.org/10.1364/AO.388993>
- Piotrowski, J., Mucha, H., Orman, Z., Pawluczyk, J., Ratajczak, J., Kaniewski, J.: Refractive GaAs microlenses monolithically integrated with InGaAs and HgCdTe photodetectors. *Proc. Spie*. **5074**: 918-925 (2003). <https://doi.org/10.1117/12.511997>
- Qiu, W.C., Hu, W.D., Chen, L., Lin, C., Cheng, X.A., Chen, X.S., Lu, W.: Dark Current Transport and Avalanche Mechanism in HgCdTe Electron-Avalanche Photodiodes. *IEEE Trans. Electron Devices*. **62**, 1926 (2015). <https://doi.org/10.1109/TED.2015.2417193>
- Robert, H.H.: Single-photon detectors for optical quantum information applications. *Nat. Photonics*. **3**, 696 (2009). <https://doi.org/10.1038/nphoton.2009.230>
- Selberherr, S.: *Analysis and Simulation of Semiconductor Devices*. Springer-Verlag Wien (1984). <https://link.springer.com/book/10.1007%2F978-3-7091-8752-4>
- Sun, S.L., He, Q., Xiao S., Li, X., Zhou, L.: Gradient-index meta-surfaces as a bridge linking propagating waves and surface waves. *Nat. Mater*. **11**, 426 (2012). <https://doi.org/10.1038/nmat3292>
- Wen, J., Wang, W.J., Li, N., Li, Z.F. Lu, W.: Light enhancement by metal-insulator-metal plasmonic focusing cavity. *Opt. Quantum Electron*, **48**, 150 (2016). <https://doi.org/10.1007/s11082-016-0399-z>
- Wen, J., Wang, W.J., Li, N., Lu, W.: Plasmonic optical convergence microcavity based on the metal-insulator-metal microstructure. *Appl. Phys. Lett*. **110**, 187901 (2017). <https://doi.org/10.1063/1.4984921>
- Yu, C., Shangguan, M.J., Xia, H.Y., Zhang, J., Dou, X.K., Pan, J.W.: Fully integrated free-running InGaAs/InP single-photon detector for accurate lidar applications. *Opt. Express* **25**, 14611 (2017). <https://doi.org/10.1364/OE.25.014611>

Figures

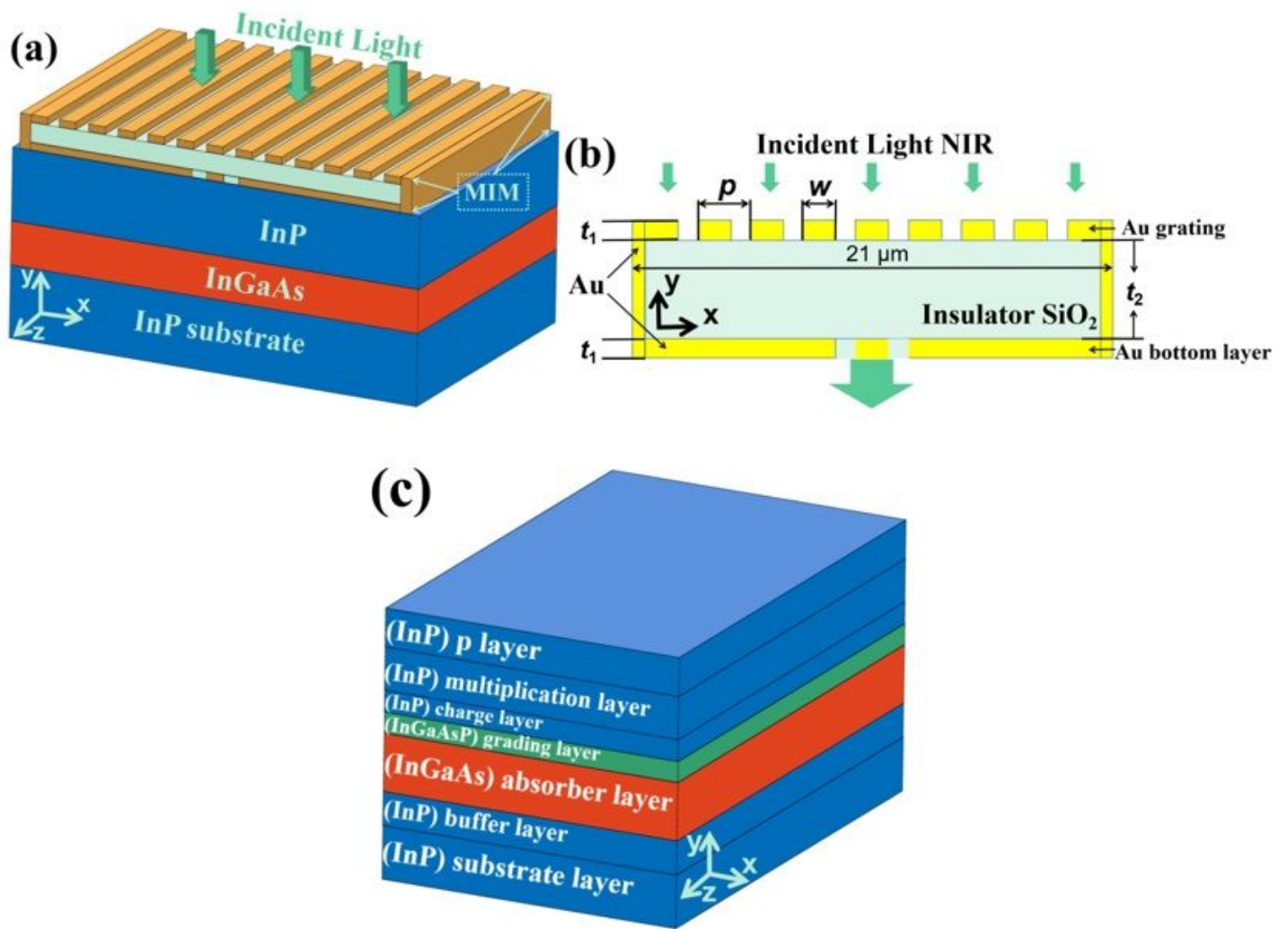


Figure 1

a Schematic diagram of the MIM-APD structure, light incident along the -y-direction. b The xOy cross-sectional schematic diagram of the MIM structure. c Schematic diagram of APD electrical simulation structure.

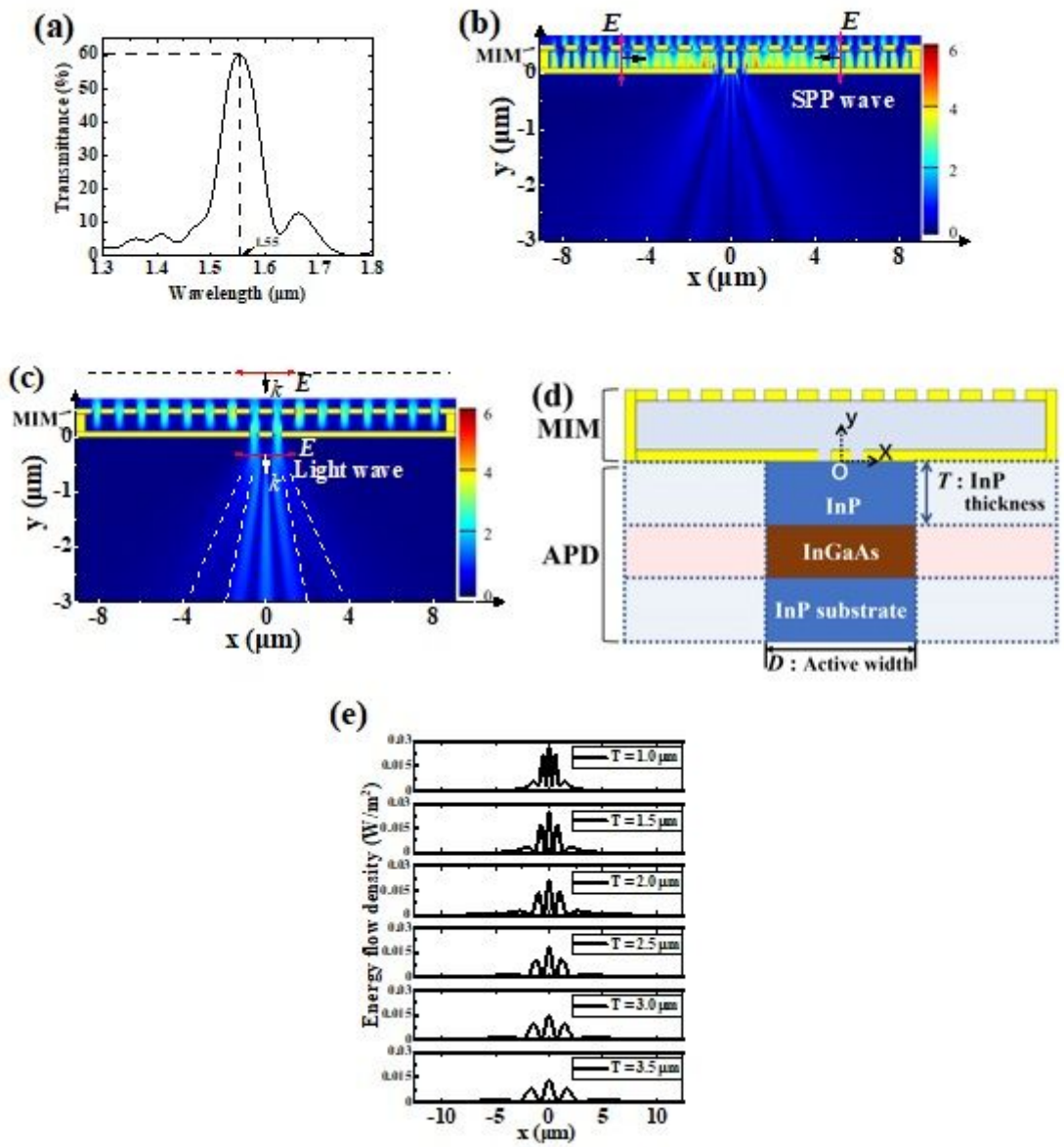


Figure 2

a Simulated transmission spectrum of 2D simulation of MIM structure. b The distribution of the electric field $|E_y|$ at 1550 nm. c The distribution of the electric field $|E_x|$ at 1550 nm. d A schematic diagram of the xOy cross-section structure of the MIM-

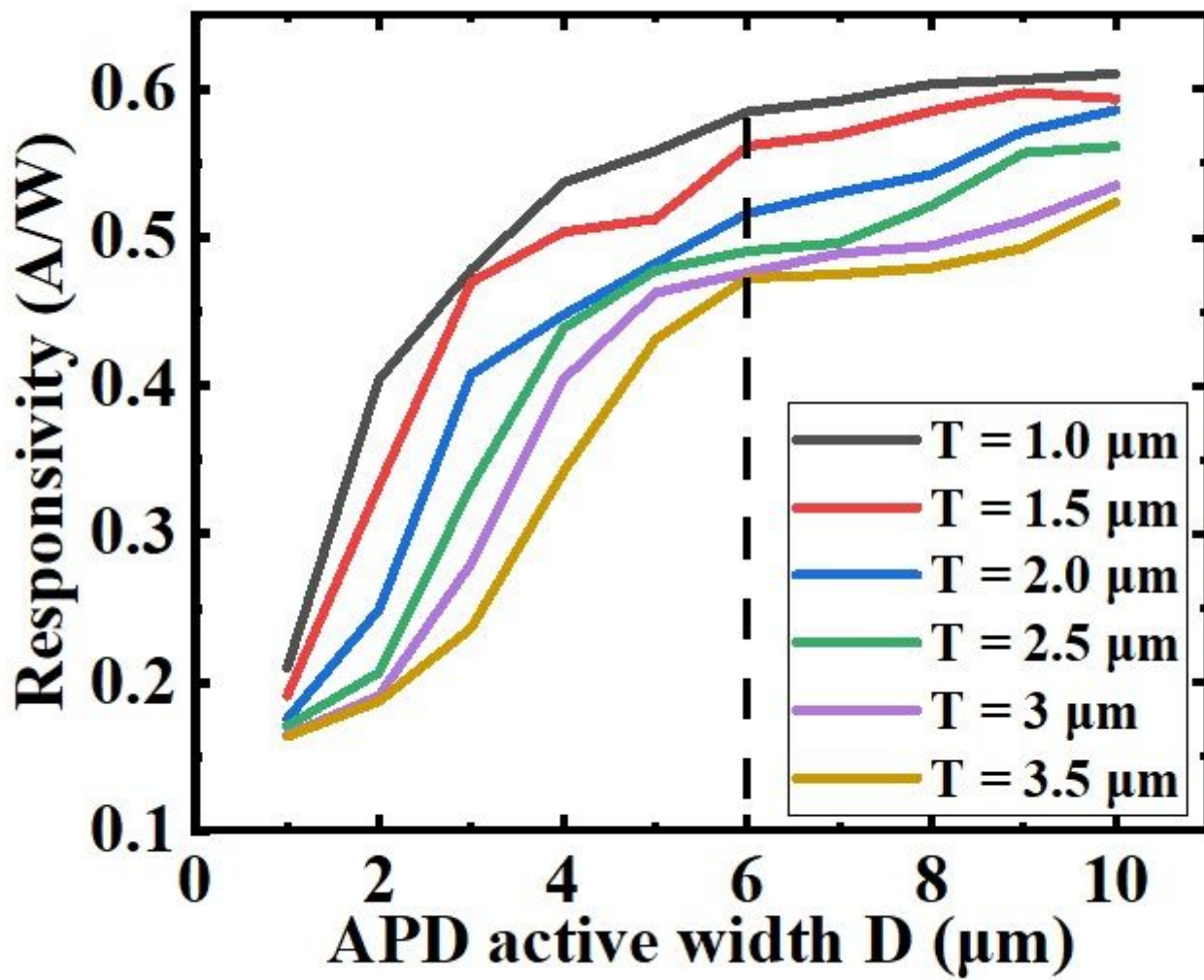


Figure 3

The photoresponsivity of MIM-APD vs APD active width D and InP thickness T.

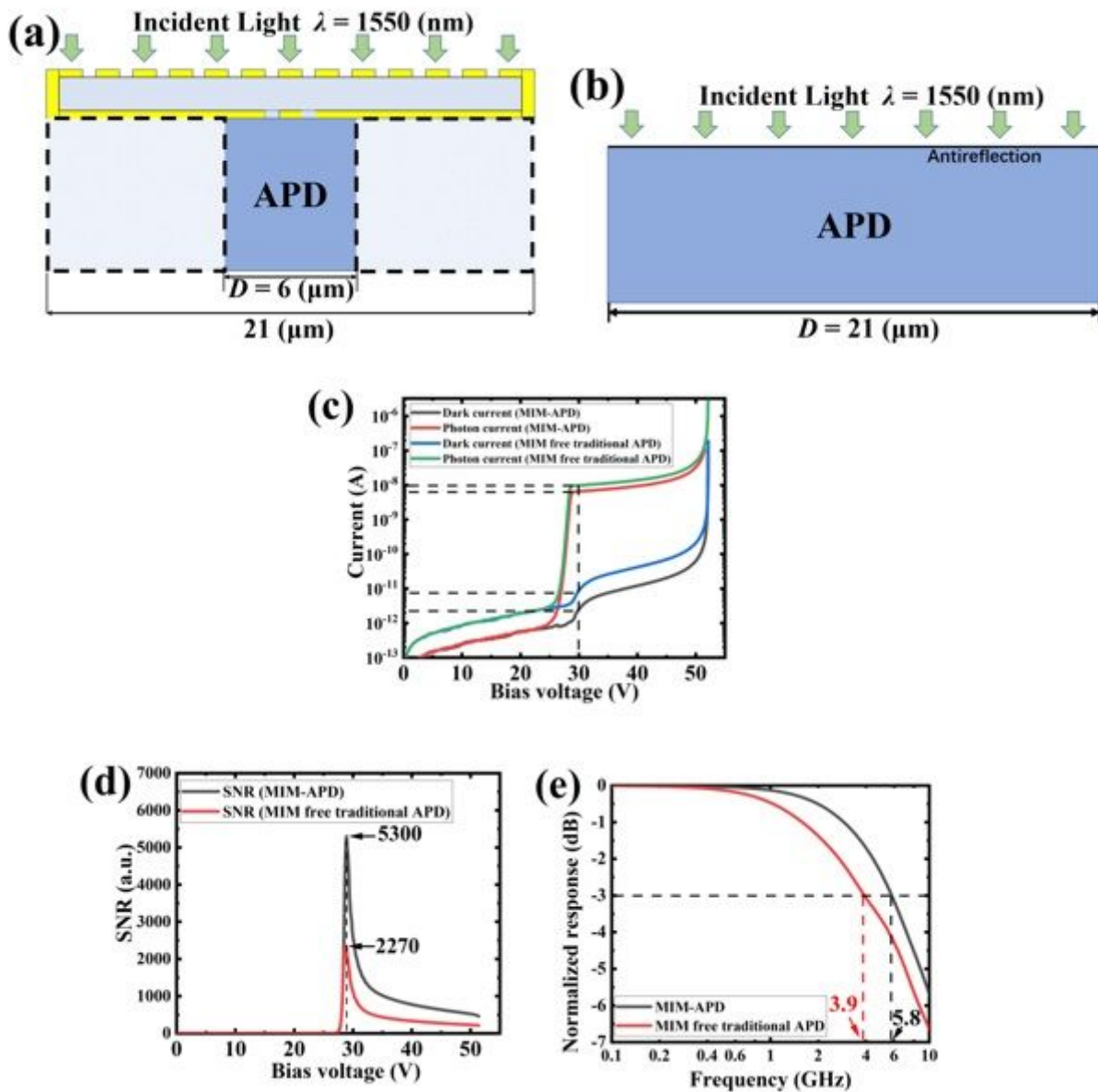


Figure 4

a Schematic diagram of simulated MIM-APD 2D structure, the active width $D = 6$ μm , and the width of the upper MIM is 21 μm . b Schematic diagram of simulated MIM free traditional APD 2D structure, the APD active width $D = 21$ μm , and coated antireflection on its surface. c The I-V curves of MIM-APD and MIM free traditional APD. d The SNR of MIM-APD and MIM free traditional APD. e The normalized photoresponses of MIM-APD and MIM free traditional APD .

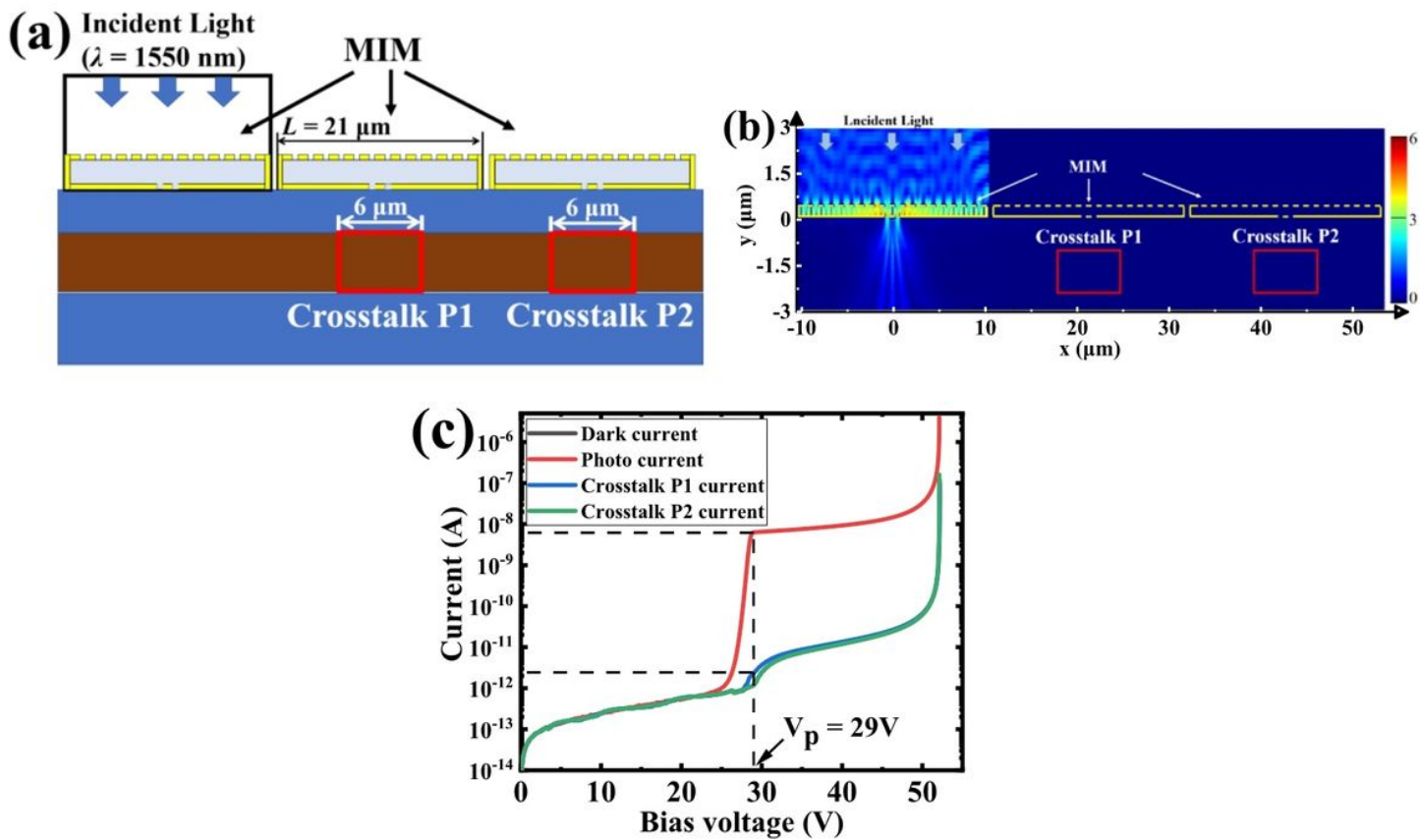


Figure 5

a The diagram of three MIM-APD pixels structure in optical crosstalk simulation. b Simulated optical field distribution $|E|$ of MIM-APD. c The I-V curves for crosstalk of APD are taken from the simulation, the black line and the red line are the APD dark current and the photocurrent of the APD in first pixel.